Electronic Supplemental Information (ESI)

Microfluidic-Prepared, Monodisperse, X-ray-Visible, Embolic Microspheres for Non-Oncological Embolization Applications

Cyrus W. Beh‡[a,b], Yingli Fu‡[c], Clifford R. Weiss[c], Charles Hu[d], Aravind Arepally[e], Hai-Quan Mao[d], Tza-Huei Wang*[a,f], and Dara L Kraitchman*[c]

a Department of Biomedical Engineering, Johns Hopkins University. 3400 N. Charles St, Baltimore, MD 21218
b Institute of Bioengineering and Nanotechnology, A*STAR, Singapore
c Russell Morgan Department of Radiology and Radiological Science, Johns Hopkins University School of Medicine. 600 N Wolfe St, Park 314, Baltimore, MD 21287
d Department of Material Science and Engineering, Johns Hopkins University.
e Department of Radiology, Piedmont Healthcare, Atlanta, GA
f Department of Mechanical Engineering, Johns Hopkins University. 3400 N. Charles St, Baltimore, MD 21218
 ‡ C.W. Beh and Y. Fu contributed equally

Design of Microfluidic Device

Supplementary Figure 1 shows the design of microfluidic device. The nozzles are arranged as follows – the alginate source is split into four parallel streams, then linearly into 5 streams, and finally into two parallel streams, thus yielding 40 nozzles. This arrangement is the result of needing to fit the device on a smaller footprint. The linear distribution is only true when the streams are split into 5, and resistance elements in the form of serpentine channels are introduced to reduce the pressure drop.
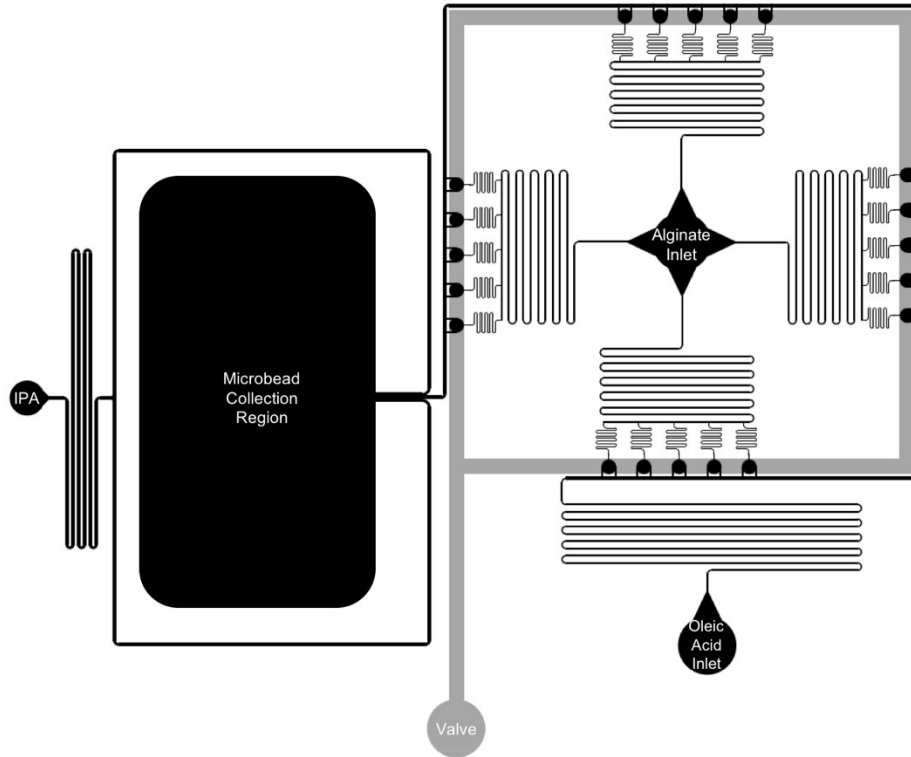

Supplementary Figure 1 Design of microfluidic device. The alginate stream is split into 40 nozzles, and side-sheared by the calcified oleic acid to form the droplets, and fully crosslinked with the IPA containing calcium chloride. The valve is pressurized during the whole process, depressing the 20 circular valve pads that constitute the pseudo-check valves. Narrow serpentine channels are used to create high resistance elements, which reduce the pressure drop across the linearly-arranged elements. In this way, the effective pressure drop across the nozzles and oleic acid channel are only around 2% and 6%, respectively. An on-chip microbead collection region is cut out, into which the exiting beads are collected.

Experiments and COMSOL Model to Determine Parameters that Influence Bead Diameter

To examine the dependence of bead diameter on alginate flow rate, a computational model of the droplet generation process was created using COMSOL. A two-phase flow level set model was used to investigate the relationship between droplet size and alginate flow rate in a T-junction side-shearing droplet generator (Fig. S1 A). The parameters used were as follows:

|	
Viscosity of alginate, mPa-s	50
Viscosity of oleic acid, mPa-s	27.64
Flow rate of alginate, nL/s	0.3-2.4
Flow rate of oleic acid, nL/s	30
Surface tension, mN/m	7
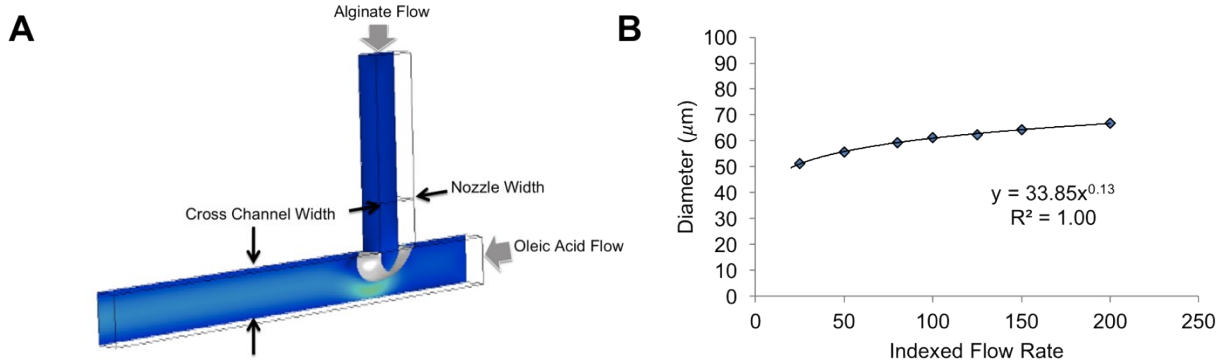
Supplementary Figure 2 COMSOL modeling of droplet/microbead generation. (A) The T-junction model is re-created in the computational model, and parameters used are based on the experimental conditions. (B) The relationship between the flow rate and bead diameter was studied, and is comparable to the experimental results (exponent of 0.13 vs 0.14 in the empirical results), which suggests the veracity of the model.

In addition, simulations were performed to determine the effect of cross channel and nozzle width on bead diameter. The simulations were compared to experiments performed in a single-nozzle microfluidic device with nozzle dimension of 50 x 25 µm, and an 80 x 80 µm cross channel while varying the alginate pressure (4-15 psi). High-speed videos (Casio Exilim EX-F1 camera) of the bead generation were analyzed (ImageJ) to determine the bead diameters, generation frequency, and flow rates of both the alginate and oleic acid.

It is well-known that the dynamics of droplet generation on microfluidic devices are determined largely by the capillary number,

$$Ca = \mu v/\gamma$$

where µ and v are the viscosity and the velocity of the continuous phase, respectively, and γ is the surface tension between the two phases.[1-3] The capillary number is a measure of the relative dominance of the viscous forces (when Ca is large) or interfacial forces (when Ca is small). For our experiments, the capillary number is on the order of 1.5 x 10^{-2}, and can be considered to operate between the so-called 'squeezing' and 'dripping' regimes of droplet generation.[4, 5] Using this model, we have investigated the effect of fluctuations in the alginate flow rate on the droplet diameter. Our findings suggest that the droplet diameter is weakly dependent on the alginate flow rate (Supplementary Figure 1 B, exponent ~0,13), in agreement with the empirical results (Main Text, Figure 3D), as well as previously-published results.[6, 7]
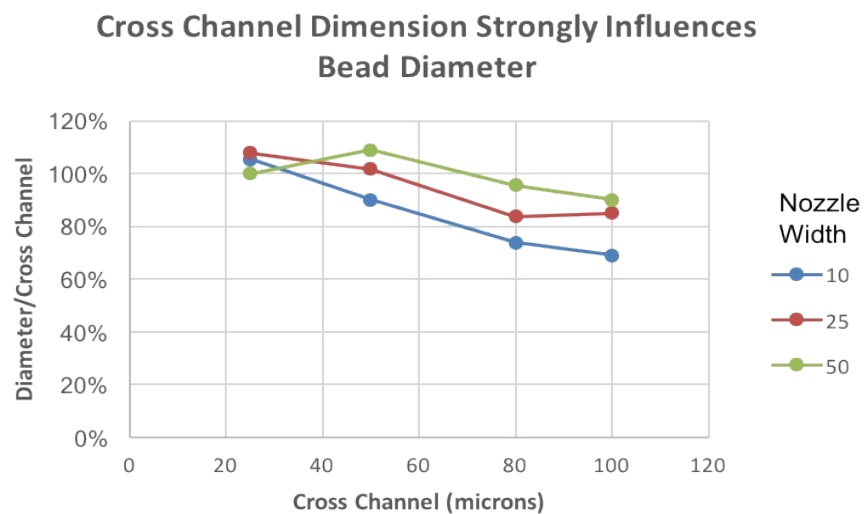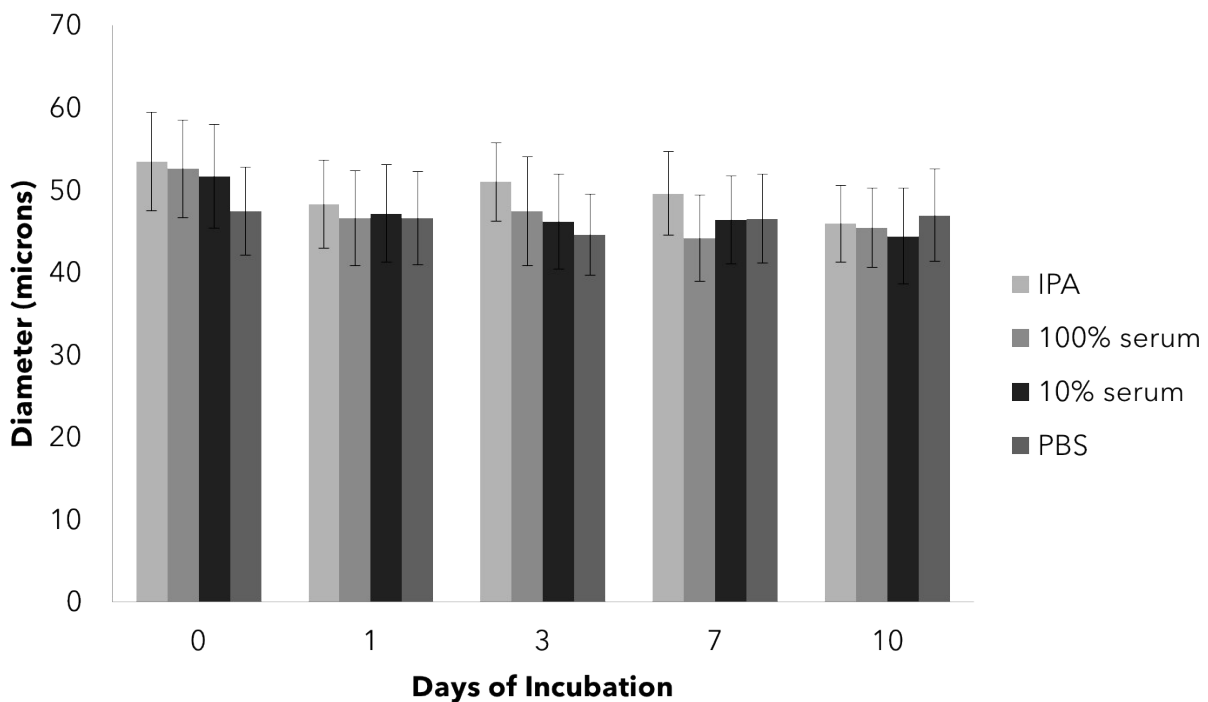

Supplementary Figure 3 Bead diameter as a percentage of cross channel width. The diameter of the microbeads is most strongly influenced by the size of the cross channel. This may be because the pinch-off of the droplet depends on the pressure built up by the continuous phase, which is in turn determined by the extent of occlusion of the cross channel. This occlusion is similar for a given cross channel dimension, regardless of the nozzle size.

The model also allows us to quickly test a variety of channel dimensions, and we found that the bead diameter is most strongly influenceed by the cross channel width, and to a lesser extent, the nozzle size. While the physics behind the generation is surprisingly complex,[4, 5, 7] the model offers us a way to design devices with the appropriate channel dimensions to achieve different microbead sizes.

Microbead Stability in Serum

Since the embolic beads are intended to remain in the vessels for long periods of time, their stability in solution, and in particular serum, is of interest. To test the microbead stability, we incubated them at 37°C in PBS, 100% serum, or 10% serum. Stability was determined based on measured microscopic diameter using an optical microscope and shape changes (ImageJ, n=150 beads) after 0, 1, 3, 7 and 10 days (Supplementary Figure 3). In all cases, there was no significant change in the bead diameter after one day incubation, attributed to the small size of the beads permitting equilibrium to be reached very quickly. Microbeads stored in IPA/calcium buffer at 4°C were evaluated at 18 months for changes in size.


Supplementary Figure 4 IEB stability. Incubation of the IEBs in calcified isopropyl alcohol (IPA), 100 % serum, 10 % serum, and phosphate buffer solution (PBS) showed that they are stable for at least 10 days at 37 °C. Bead diameter was determined by image analysis of 150 beads for each condition.

Renal Arterial Embolization

Selective renal artery embolization was performed in healthy growing swine under general anesthesia using X-ray fluoroscopy guidance. Using a Seldinger technique under ultrasonic guidance, percutaneous femoral artery access in pigs was achieved by placing a 5 Fr introducer sheath. A 5 Fr high-flow angiographic catheter (SOS Omni Selective Catheter, Angiodynamics) was advanced from the femoral artery via the aorta to select either the left or right kidney, and a DSA (63 kV, 320 mA, 3 frames/s, 32 cm FOV, and manual iohexol injection) was acquired of the selected kidney. A microcatheter (Renegade Hi-Flo, Boston Scientific Corp.) was advanced over a 0.016" steerable wire (Fathom, Boston Scientific Corp.) into either the inferior or superior pole of the kidney using the DSA roadmap. A DSA was then obtained of the selected kidney pole. XEMs (~0.1 ml) suspended in saline were then injected without iodinated contrast into the microcatheter during direct fluoroscopic visualization (e.g., DSA). Persistence of the XEMs was evaluated on fluoroscopic image. In acute studies, the microcatheter was removed and flushed outside the body and repositioned in the contralateral kidney. A DSA was acquired and the microcatheter was advanced into the

selected kidney pole and conventional embolic beads (Embozene) mixed with iohexol were injected under direct fluoroscopic visualization until stasis was achieved. The catheters were then removed, and, using a pigtail catheter in the aorta at the level of the renal arteries, a DSA CBCT (DynaCT, 8 s digital subtraction angiogram (DSA), 48 cm FOV, 0.5°/step, 210° rotation, 94 kV, and 475 mA) was obtained during injection of iohexol (5 ml/s for 12 seconds) was obtained of both kidneys to confirm embolization.   For acute studies, the animal was humanely euthanized, and the kidneys were harvested for gross and histopathological examination.
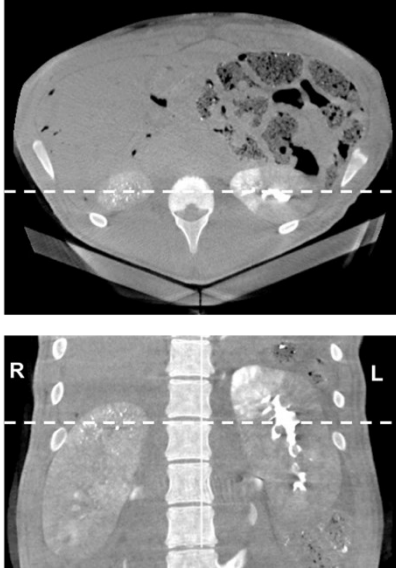
Supplementary Figure 5 Coronal view of CBCT image of the swine whose left kidney (L) was embolized with conventional embolic beads mixed with iodinated contrast agent and right kidney (R) was embolized with XEMs.   The right kidney embolized with XEMs shows punctate radiopacities in the superior pole representing XEMs whereas the conventional embolics show generalized radiopacity of the superior pole related to trapping of the radiopaque contrast by the embolic. With additional time for washout of the iodinated contrast agent, the conventional embolic would no longer be visible on follow-up CT.

Bariatric arterial embolization (BAE)

After optimizing the handling and imaging properties of these XEMs, we examined their embolization effect on BAE, a novel treatment for obesity where non-target embolization (NTE) would be unacceptable. Ten healthy growing swine were randomized to receive either XEMs (acute: n = 3; chronic: n = 4) or a sham procedure (n = 3) using minimally invasive percutaneous approach.[8] Percutaneous access to the femoral artery was achieved in pigs under general anesthesia with isoflurane. A 5 Fr introducer sheath was placed using a Seldinger technique under ultrasonic guidance. Under X-ray fluoroscopic guidance, a 5 Fr angiographic guide catheter (Mickelson, Angiodynamics) was advanced from the femoral artery over a guide wire into the abdominal aorta to select the celiac axis and obtain a pre-embolization DSA to identify the vessels feeding the gastric fundus. A microcatheter (Renegade Hi-Flo, Boston Scientific Corp.) was advanced over a 0.016" wire (Fathom, Boston Scientific Corp.) into the fundal branches of the gastric artery. A DSA of the selected vessels was then obtained, followed by a CBCT during a 25% iohexol injection using parameters similar to those of renal CBCT. If, at the appropriate location, XEMs embolization (0.05–0.1 ml) was performed during direct fluoroscopic visualization and a post-embolization CBCT without contrast was obtained. The microcatheter was then removed and repositioned to perform XEMs embolization in any additional fundal arterial branches, i.e., typically 1-2 additional vessels. For chronic studies, the catheters and femoral sheath were removed and direct pressure was applied to the femoral artery to obtain hemostasis. The animal was then allowed to recover. Repeat CBCTs and weights were obtained on a weekly basis under general anesthesia.   All animals were humanely euthanized prior to harvest of the stomach, liver, pancreas, and spleen.

Supplementary Figure 6 Endoscopic view of the stomach receiving XEM embolization in three major fundal arteries showing gastric ulcerations with fibrin caps (yellow). The ulceration was likely attributed to overembolization-induced ischemic damage in the gastric mucosa.

Only the animal that received embolization in three fundal vessels showed ulceration, attributed to extensive ischemic damage (Supplementary Figure 6). Gross examination of the post-mortem stomach for this animal at four weeks post embolization revealed healing (not completely healed) ulcers in this animal; the other three chronic animals did not show any ulcers post-mortem.
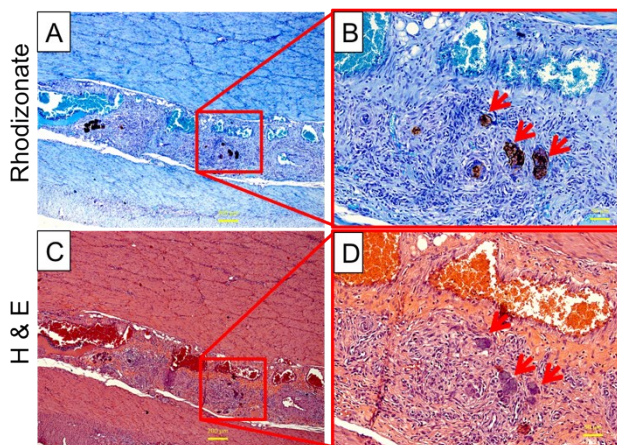
Supplementary Figure 7 Histological analysis of treated stomach tissue. **A, B**: Rhodizonate staining for barium particles presence (arrows) reveals XEMs in submucosa of gastric fundus of BAE swine. **C, D**: XEMs are visible in corresponding region (arrows) of the same tissue stained with hematoxylin and eosin (H&E). Bars represent 200 μm for A, C and 50 μm for B, D.

Hematoxylin and eosin staining and rhodizonate staining to identify barium particles were also performed on embolized stomach. Positive staining for rhodizonate was only seen in the gastric fundus and in conjunction with areas containing XEMs and not in other organs demonstrating successful embolization without the breakdown and loss of barium sulfate from XEMs (Supplementary Figure 7).

Supplemental Video 1. Operation of droplet generation nozzles. The pressurized valve (large circle) prevents the calcified oil from backflowing along the alginate channel. Droplet generation takes place at around 20 Hz, and the playback is slowed down 10x midway through the video for better visualization of the process.

Supplemental Video 2. Phase transfer of alginate beads into IPA-rich, high calcium crosslinking solution. The central stream is the calcified oil, carrying weakly-crosslinked alginate beads into the crosslinking region. The sheath flow configuration maintains the confinement of the bead in a single file, preventing fusion and aggregation. As the beads come into contact with the IPA-rich lateral streams, they move quickly through the carrying oil, into the side streams, which contain high calcium for complete crosslinking.

Supplemental Video 3. XEM Injection in Swine Kidney. Digital subtraction angiogram (DSA) of X-ray-visible embolic microspheres (XEMs) selective injection in the superior pole of a swine kidney is visible without the additional of iodinated contrast enabling the visualization of target and non-target embolization as seen in single frame images of Fig. 4A-F.

Supplementary References:

1.   H. Gu, M. H. G. Duits and F. Mugele, *International Journal of Molecular Sciences*, 2011, **12**, 2572-2597.
2.   J. D. Tice, A. D. Lyon and R. F. Ismagilov, *Analytica Chimica Acta*, 2004, **507**, 73-77.
3.   J. D. Tice, H. Song, A. D. Lyon and R. F. Ismagilov, *Langmuir*, 2003, **19**, 9127-9133.
4.   P. Garstecki, M. J. Fuerstman, H. A. Stone and G. M. Whitesides, *Lab on a Chip*, 2006, **6**, 437-446.
5.   M. DE MENECH, P. GARSTECKI, F. JOUSSE and H. A. STONE, *Journal of Fluid Mechanics*, 2008, **595**, 141-161.
6.   H. Liu and Y. Zhang, *Journal of Applied Physics*, 2009, **106**, 034906-034908.

7. G. F. Christopher and S. L. Anna, *Journal of Physics D: Applied Physics*, 2007, **40**, R319.
8. Y. Fu, C. R. Weiss, K. Paudel, E. J. Shin, D. Kedziorek, A. Arepally, R. A. Anders and D. L. Kraitchman, *Radiology*, 2018, **289**, 83-89.